

Green Chemistry

Accepted Manuscript



This is an *Accepted Manuscript*, which has been through the Royal Society of Chemistry peer review process and has been accepted for publication.

Accepted Manuscripts are published online shortly after acceptance, before technical editing, formatting and proof reading. Using this free service, authors can make their results available to the community, in citable form, before we publish the edited article. We will replace this *Accepted Manuscript* with the edited and formatted *Advance Article* as soon as it is available.

You can find more information about *Accepted Manuscripts* in the [Information for Authors](#).

Please note that technical editing may introduce minor changes to the text and/or graphics, which may alter content. The journal's standard [Terms & Conditions](#) and the [Ethical guidelines](#) still apply. In no event shall the Royal Society of Chemistry be held responsible for any errors or omissions in this *Accepted Manuscript* or any consequences arising from the use of any information it contains.



www.rsc.org/greenchem

Cite this: DOI: 10.1039/c0xx00000x

www.rsc.org/xxxxxx

Paper

Core–Shell Cu@(CuCo-alloy)/Al₂O₃ Catalysts for the Synthesis of Higher Alcohols from Syngas

Wa Gao,^{‡a} Yufei Zhao,^{‡b} Haoran Chen,^a Hao Chen,^a Yinwen Li,^a Shan He,^a Yingkui Zhang,^a Min Wei,^{*a} David G. Evans^a and Xue Duan^a

Received (in XXX, XXX) Xth XXXXXXXXXX 20XX, Accepted Xth XXXXXXXXXX 20XX

DOI: 10.1039/b000000x

Abstract: Production of higher alcohols from the catalytic conversion of synthesis gas (CO + H₂) is one of the most promising approaches for the utilization of nonoil resources, in which bimetallic catalysts based on Cu and Fischer–Tropsch (FT) reaction active elements (e.g., Co, Fe, Ni) are efficient and cost-effective candidates. Herein, we demonstrate the fabrication of core–shell Cu@(CuCo-alloy) nanoparticles (NPs) embedded on a Al₂O₃ matrix via an *in situ* growth of CuCoAl-LDHs nanoplatelets on aluminum substrates followed by a calcination-reduction process, which serve as an efficient catalyst toward CO hydrogenation to produce higher alcohols. The composition, particle size and shell thickness can be tuned by changing the Cu/Co molar ratio in the LDHs precursors, and the best catalytic behavior was obtained over the Cu/Co (1/2) catalyst with a CO conversion of 21.5% and a selectivity (C₆₊ slate 1-alcohols) of 48.9%, which is superior to the traditional modified FT catalysts. The XPS, *in situ* FTIR spectroscopy and HAADF-STEM reveal that the unique electronic and geometric interaction between Cu and Co in the Cu@(CuCo-alloy) NPs give contribution to the significantly enhanced catalytic performances. In addition, the 3D hierachical structure of Cu@(CuCo-alloy)/Al₂O₃ catalyst facilitates the mass diffusion/transportation as well as prevents the hotspot formation, accounting for its stability and recyclability. The Cu@(CuCo-alloy)/Al₂O₃ catalyst with significantly improved catalytic behavior can be potentially used in CO hydrogenation to produce higher alcohols.

1. Introduction

Limited crude oil reserves and competition with the food industry associated with fermentation-based biofuel production inspire new efforts on effective catalytic transformations of alternative carbon sources to produce energy carriers and chemical feedstocks.¹ Production of higher alcohols from the catalytic conversion of synthesis gas (CO + H₂) derived from coal, natural gas, or renewable biomass is one of the most promising approaches for utilizing nonoil resources cleanly and efficiently.^{1,2} Although Rh-based catalysts are effective for the formation of ethanol and other C₂₊ oxygenates from syngas, the very high cost of Rh prohibits its large scale utilization.³ Recent research interest has been focused on the employment of nonprecious metal catalysts to produce higher alcohols from syngas over transition metal catalysts (e.g., Cu-Co, Cu-Fe systems),⁴ but improvements in the overall catalytic activity, alcohol selectivity, and long-term stability of these materials are highly necessary.

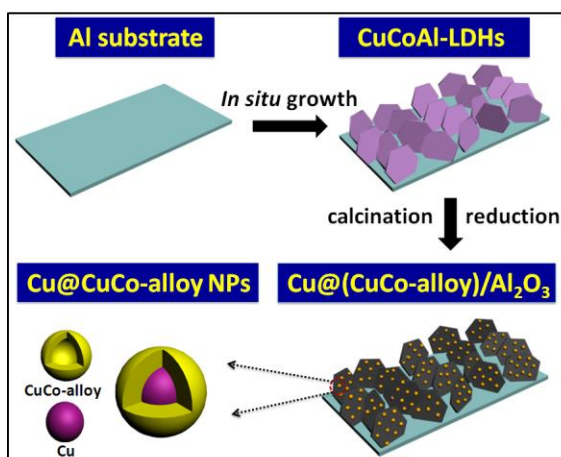
Bimetallic catalysts, composed of two metal elements in either alloys or intermetallic compounds, emerge as a new materials category with unique catalytic properties different from monometallic catalysts through modification of electronic and/or structural factors.⁵ For the production of higher alcohols from

syngas, bimetallic catalysts based on Cu and Fischer–Tropsch (FT) reaction active elements (e.g., Co, Fe, Ni) have been demonstrated as one of the most promising catalysts, in which Cu species assists in non-dissociative activation of CO for the CO insertion and subsequently alcohol formation while FT active elements act as active sites to dissociate CO to form surface alkyl.^{1a,2c,3,6} A synergistic effect between these two metal compositions is believed to be essential in this reaction.^{1a,3,7} However, a phase separation of these bimetallic catalysts generally occurs during the reaction process, which would break the synergetic interaction and deteriorate the catalytic performance.⁸ Moreover, the weak thermal conductivity of these powdered catalysts will induce hotspots and cause catalytic deactivation.⁹ Therefore, the design and preparation of new bimetallic catalysts with desirable activity, selectivity and high stability toward the production of higher alcohols from syngas remain a challenging goal.

Layered double hydroxides (LDHs) are a class of naturally occurring and synthetic materials generally expressed by the formula [M²⁺_{1-x}M³⁺_x(OH)₂](Aⁿ⁻)_{x/n}mH₂O.¹⁰ The specialty of this material is that divalent and trivalent cations are uniformly distributed on the atomic scale in slabs of edge-sharing MO₆ octahedra that allow a close interaction of metal cations.¹¹ Recently, considerable interest has been focused on LDHs

materials as heterogeneous catalysts based on their versatility in chemical composition and structural architecture.¹² In particular, a topotactic transformation of LDHs materials to uniformly-dispersed metal NPs supported on metal-oxide support occurs upon calcination in a reductive atmosphere.¹³ Inspired by the structural merits of LDHs materials, we explored the idea of the incorporation of Cu element and FT reaction active Co element into the LDHs precursor on the atomic scale, so as to fabricate supported CuCo bimetallic catalysts toward CO hydrogenation *via* the topotactic transformation process.

In this work, core-shell structure Cu@(CuCo-alloy) nanoparticles (NPs) embedded on the Al₂O₃ matrix with a high dispersion (denoted as Cu@(CuCo-alloy)/Al₂O₃) were fabricated *via* a facile two-step procedure: an *in situ* growth of CuCoAl-LDHs nanoplatelets on aluminum substrates as the precursor followed by a calcination-reduction process (Scheme 1), which serve as efficient catalysts toward the CO hydrogenation to produce higher alcohols. The HRTEM and HAADF-STEM results confirm that the well-dispersed core-shell structure Cu@(CuCo-alloy) NPs with diameter of ~15 nm were embedded on the Al₂O₃ matrix. The resulting materials demonstrate significantly improved catalytic CO hydrogenation to higher alcohols, and the best catalytic behavior was obtained over the Cu/Co (1/2) catalyst with a CO conversion of 21.5% and the C₆₊ slate 1-alcohols selectivity of 48.9%, which is superior to the traditional modified FT catalysts. The unique electronic and geometric interaction between Cu and Co in the Cu@(CuCo-alloy) NPs give contribution to the significantly enhanced catalytic performance, and the bimetal phase separation is inhibited. In addition, the 3D hierarchical Cu@(CuCo-alloy)/Al₂O₃ catalyst facilitates the mass diffusion and transportation, and the substrate prevents the hotspot formation due to its high thermal conductivity. Therefore, our approach holds significant promise for bimetallic CuCo core-shell structure as a new efficient catalyst toward the production of higher alcohols from syngas.



Scheme 1. Illustration of the structured Cu@(CuCo-alloy)/Al₂O₃ catalyst with core-shell architecture derived from CuCoAl-LDHs film based on an *in situ* growth reaction followed by a calcination-reduction process.

2. Experimental Section

2.1 Catalyst preparation

Preparation of the structured CuCoAl-LDHs, CuAl-LDHs, and CoAl-LDHs film:

The CuCoAl-LDHs, CuAl-LDHs, and CoAl-LDHs film as catalyst precursors were prepared by an *in situ* crystallization on an aluminum substrate.¹⁴ The Al substrate was cleaned thoroughly with ethanol and deionized water in sequence.

In a typical procedure, 0.01 mol of Cu(NO₃)₂·3H₂O and Co(NO₃)₂·6H₂O with a given molar ratio of Cu²⁺/Co²⁺ (5/1, 2/1, 1/2, 1/5, respectively) and 0.06 mol of NH₄NO₃ were dissolved in deionized H₂O (100 mL) to obtain a clear solution, which was adjusted to pH=6.5 by adding diluted ammonia (1.5% NH₄OH). The Al substrate (15 cm × 20 cm) was placed vertically in the solution in an autoclave, which was placed in a conventional oven at 80 °C for 48 h. The substrate was then withdrawn from the autoclave, rinsed with ethanol, and dried at room temperature (denoted as CuCoAl-LDHs). The other CuAl-LDHs and CoAl-LDHs samples were prepared by a similar method with 0.01 mol of Cu(NO₃)₂·3H₂O and Co(NO₃)₂·6H₂O, respectively.

Preparation of the structured Cu@(CuCo-alloy)/Al₂O₃, Cu/Al₂O₃, and Co/Al₂O₃ catalyst:

The CuCoAl-LDHs, CuAl-LDHs, and CoAl-LDHs precursor films were calcined in air at 500 °C for 5 h with a heating rate of 2 °C min⁻¹ to obtain the mixed metal oxides (denoted as CuCoAl-MMO, CuAl-MMO, and CoAl-MMO). Subsequently, the three samples were reduced in a hydrogen atmosphere at 500 °C for 5 h with a heating rate of 2 °C min⁻¹. The final catalysts were labeled as Cu@(CuCo-alloy)/Al₂O₃, Cu/Al₂O₃, and Co/Al₂O₃.

Preparation of the powdered CuCo/Al₂O₃ catalyst:

The powdered CuCo/Al₂O₃ as a reference catalyst was prepared by a conventional impregnation method, in which the metal contents of Cu and Co were controlled to be 20wt.% and 42wt.%, respectively (see details in the SI), in accordance with those of the optimal catalyst Cu@(CuCo-alloy)/Al₂O₃ (Cu/Co=1/2). In a typical procedure, commercial γ-Al₂O₃ was used as support. Aqueous solution of Cu(NO₃)₂·3H₂O and Co(NO₃)₂·6H₂O was added dropwise into alumina support with continuous stirring, followed by aging at room temperature for 4 h. After the impregnation, the sample was calcined in air at 100 °C for 2 h and then at 500 °C for 5 h (heating rate: 2 °C min⁻¹). After hydrogen reduction at 500 °C for 5 h with a heating rate of 2 °C min⁻¹, the final catalyst was labeled as powdered-CuCo/Al₂O₃.

2.2 Characterization of samples

The X-Ray diffraction (XRD) patterns of samples were obtained on a Shimadzu XRD-6000 diffractometer, using Cu Kα radiation (λ = 0.154 nm) at 40 kV, 30 mA, a scanning rate of 5 ° min⁻¹, a step size of 0.02 ° s⁻¹, and a 2θ angle ranging from 3 to 70 °. Elemental analysis for Cu and Co was performed using a Shimadzu ICPS-75000 inductively coupled plasma emission spectrometer (ICP-ES). The sample morphology was investigated using a scanning electron microscopy (SEM; Zeiss Supra 55) with an accelerating voltage of 20 kV, combined with energy dispersive X-ray spectroscopy (EDX) for the determination of metal composition. Transmission electron microscopy (TEM) was performed using a Hitachi H-800 transmission electron microscopy operated at 100 kV. High resolution transmission

electron microscopy (HRTEM) was carried on a JEM-3010 at an accelerating voltage of 200 kV. Surface elemental analysis was performed using an ESCALAB250 X-ray photoelectron spectroscopy (XPS) equipped with Mg K α radiation. C1s peak at 284.6 eV was used as a calibration peak. The Modified Auger parameter (α') is defined as:

$$\alpha' = E_b + E_k \quad (1)$$

where E_b and E_k are the binding and kinetic energies of the dominant core electron and Auger electron line for a particular element, respectively.¹⁵

Temperature-programmed reduction (TPR) was conducted on a Micrometric ChemiSorb 2750 chemisorption instrument with a thermal conductivity detector (TCD). About 100 mg of samples was loaded in a quartz reactor. TPR was carried out with a heating ramp rate of 5 °C min⁻¹ in a stream of 10% H₂ in Ar to a sample temperature 800 °C, with a total flow rate of 25 mL min⁻¹.

In situ Fourier-transformed infrared absorption (FT-IR) spectroscopy of CO experiment was carried out in a quartz cell equipped with KBr windows allowing sample activation and successive measurements in the range of 25–600 °C, at a pressure as low as 10⁻⁴. About 50 mg of the sample was pressed into a disk and activated in the same cell used for the measurement. The thermal treatment was performed either in dynamic vacuum or under static conditions, according to procedures discussed below.

FT-IR spectra were collected with Nicolet 380 instrument spectrophotometer at a spectra resolution of 4 cm⁻¹ and accumulation of 64 scans. After nitrogen pre-treatment at 200 °C for 60 min and hydrogenation treatment at 500 °C for 60 min, the sample was scanned to get a background record below a pressure of 2×10⁻⁴ Pa. Subsequently, the sample was exposed to a CO flow at 30 °C for another 120 min. Sample scanning for adsorbed CO on the studied sample was conducted after the pressure was reduced below 2×10⁻⁴ Pa again.

2.3 Catalytic evaluations

Carbon monoxide hydrogenation reaction was carried out in a fixed bed stainless steel tubular microreactor (8 mm in diameter, 500 mm in length). The structured catalyst was rolled and placed vertically in the stainless steel tubular microreactor. The total Cu@(CuCo-alloy)/Al₂O₃ catalyst on the Al substrate was ~1.2 g. The temperature of the reactor was controlled *via* a temperature controller. H₂, CO and N₂ were purged into the reactor at a desired rate by mass flow controllers. Nitrogen was used as an internal standard gas in the reactor feed. Prior to reaction, the catalyst was reduced *in situ* in a flow of H₂ (40 ml/min) under atmospheric pressure at 500 °C for 5 h. The reactor was cooled down to 220 °C and synthesis gas with a flow rate of 40 mL/min (H₂: CO=2.0, v/v) was introduced to increase the pressure to 2.0 MPa. During the process, the total pressure in the system was kept at 2.0 MPa (H₂/CO=2.0, v/v) with the space velocity of 2000 ml/g_{cat}/h. The outlet gas components (CO, H₂, CH₄, CO₂ and N₂) were determined using an online GC-2014C Shimadzu gas chromatograph by TCD detector (TDX-1 column). The liquid alcohol and hydrocarbons products were captured using an ice-water bath and analyzed off-line with the same chromatograph (a PEG-20 M capillary column and a FID detector Porapak Q column).

3. Result and discussion

3.1 Structural and morphological study of the catalysts

The Fig. 1A illustrates the XRD patterns of the CuCoAl-LDHs film (Cu/Co=1/2) obtained by the *in situ* growth method on Al substrate as well as the corresponding powdered sample scraped from the substrate for comparison. For the CuCoAl-LDHs film (curve a), a weak reflection was observed at 2θ 35.1°, which can be attributed to the [012] reflection of the LDHs phase; the strong reflection appears originating from the Al substrate.^{13,16} The XRD pattern of the powdered material scraped from the LDHs film (curve b) shows a series of reflections at 2θ 11.7°, 23.5°, 35.1°, 61.0° and 62.5°, corresponding to the [003], [006], [012], [110] and [113] reflection of an LDHs phase, respectively, which demonstrates the formation of CuCoAl-LDHs film on the Al substrate.¹¹ The morphology of the LDHs film revealed by SEM is shown in Fig. 1B and 1C. Top-view and side-view of the LDHs film show uniform hexagonal plate-like microcrystals with diameter of ~4 μm and thickness of 10–20 nm, whose *ab*-plane is perpendicular to the substrate. This is consistent with the XRD results in Fig. 1A. Calcination of the LDHs precursor leads to its transformation to mixed metal oxides (CuCoAl-MMO) (Fig. 1D, curve a), in which a CuO crystalline phase (JCPDS 89-5899) and a Co₃O₄ phase (JCPDS 78-1970) are identified in the XRD pattern. The final structured Cu@(CuCo-alloy)/Al₂O₃ catalyst was subsequently obtained *via* a reduction process of CuCoAl-MMO (see Scheme 1). As shown in Fig. 1D (curve b), a broad reflection at 2θ 44.1° is observed, which can be attributed to the superimposition of the Cu(111) and Co(111) reflection. This indicates the formation of CuCo alloy to some extent during the reduction process. According to the phase diagram of binary Co–Cu, only a maximum of 9at.% Cu can be dissolved in Co metal.¹⁷ Therefore, the metal Cu, Co and CuCo alloy may coexist in the final structured sample, which will be further discussed in the next section.

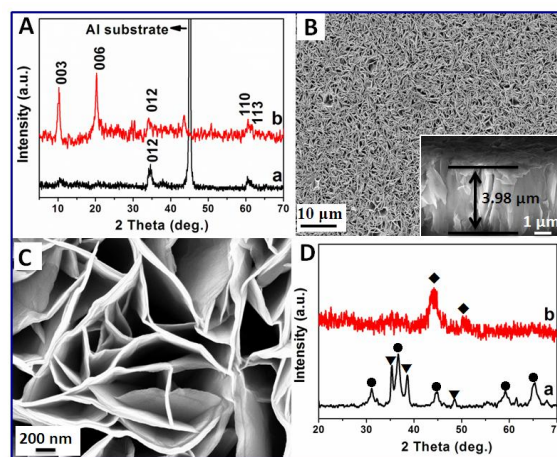


Fig. 1 (A) XRD patterns of: (a) the as-prepared CuCoAl-LDHs (Cu/Co=1/2) film, (b) the corresponding powdered material scraped from the film. (B and C) SEM images of the as-prepared CuCoAl-LDHs film (the film thickness is shown in the inset of B). (D) XRD patterns of: (a) CuCoAl-MMO, (b) the final reduction sample. Crystalline phase: (●) Co₃O₄, (▼) CuO, (◆) CuCo.

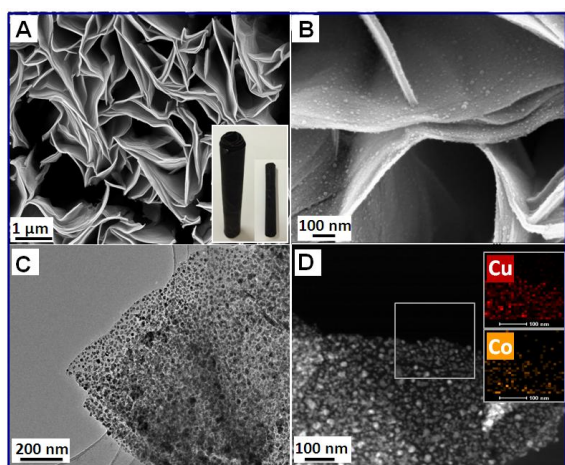


Fig. 2 (A and B) SEM images of the Cu@(CuCo-alloy)/Al₂O₃ sample (Cu/Co=1/2); the inset in A shows the photograph of the rolled Cu@(CuCo-alloy)/Al₂O₃ film catalyst. (C) TEM image of the Cu@(CuCo-alloy)/Al₂O₃ sample. (D) HAADF-STEM image of the Cu@(CuCo-alloy) NPs dispersed on the Al₂O₃ matrix with the Cu and Co EDS mapping (inset).

The architectural feature of the final reduction sample was revealed by SEM (Fig. 2A), in which the sample inherits the original flake morphology of the LDHs precursor, and no agglomeration or sintering of adjacent nanoflakes was observed. Notably, numerous well-dispersed NPs with a rather high density on the Al₂O₃ matrix are observed in Fig. 2B and 2C. The high-angle annular dark field microscopy (HAADF-STEM) and the corresponding energy-dispersive spectroscopy (EDS) mapping demonstrate that both Cu and Co element have a uniform and homogeneous distribution (Fig. 2D). The detailed structural feature of the obtained well-dispersed NPs was further revealed by HRTEM and HAADF-STEM. The HRTEM image (Fig. 3B) of a nanoflake reveals that the NPs (15–20 nm in diameter) possess a core-shell structure, in which a round core and an uneven shell (thickness: 2.4–3.5 nm) can be recognized. According to the lattice distance of 0.209 nm, the core is determined to be metal Cu (Fig. 3C).¹⁸ However, the shell is not uniform; several interconnected parts with different lattice spacings (e.g., 0.206, 0.252, or 0.302 nm) are identified, which can be assigned to the CuCo alloy phase and some tiny CoO phase.¹⁹ This suggests that in the bimetallic CuCo sample, metal Cu exists in the core section while a CuCo alloy phase accompanied with tiny CoO phase are located in the exterior shell. To get a further insight into the structure of the core-shell NPs, EDS analysis was applied to characterize the structure and composition of a typical NP. The analysis depth of EDS is 0.5–3.0 μm, which can detect the whole Cu@(CuCo-alloy) nanoparticle. As shown in Fig. 3D, the Cu signal is mainly detected in the central zone; while both Cu and Co signal are observed in the shell (Fig. 3D, inset). The results provide a striking demonstration of the core-shell structure: the metal Cu in the core and both of the two elements in the Co-dominated outer shell. This suggests that CuO is firstly reduced to metallic Cu nanoparticle during the reduction process of CuCoAl-MMO (see Fig. 8), which serves as the core for the further reduction of Co₃O₄ to metallic Co. Meanwhile, partial Cu atoms migrate to the surface to form CuCo-alloy shell, due to the relatively lower surface energy of Cu compared with Co (1.9 J m⁻² vs. 2.7 J

m⁻²).¹⁷ It has been discussed above that for Cu–Co bimetallic system, only a maximum of 9 at.% Cu can be dissolved in Co metal to form CuCo alloy. Therefore, the formation of core-shell structure (Cu as the core and CuCo alloy as the shell) would facilitate a maximum CuCo alloy. Moreover, this specific structure improves the unique electronic and geometric interaction between Cu and Co species and effectively avoids phase separation in the catalytic reaction, which will be discussed in the next section. In contrast, no obvious core-shell structure is observed for the powdered-CuCo/Al₂O₃ sample (Fig. S1B and S1C). Separate Cu, CoO and Co₃O₄ phase are observed, implying a phase separation occurs during the reduction process. The results indicate that a uniform distribution of metal elements in the LDHs precursor is necessary for the growth of Cu nanoparticle core and the subsequent CuCo-alloy shell in the Cu@(CuCo-alloy)/Al₂O₃ catalyst. This is successfully demonstrated in the LDHs precursor approach while not available in the conventional impregnation method.

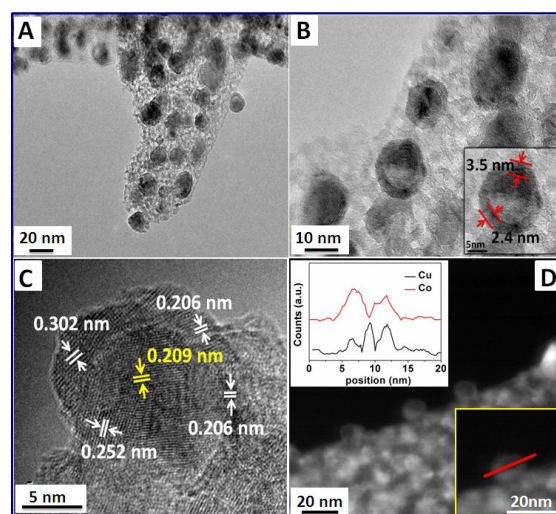


Fig. 3 Structural features of Cu@(CuCo-alloy)/Al₂O₃ (Cu/Co=1/2) sample: (A) a low magnification TEM; (B) a high magnification TEM; (C) HRTEM of a single Cu@(CuCo-alloy) NP; (D) HAADF-STEM for a single Cu@(CuCo-alloy) NP with the EDS line scan profile along the pink line; the black and red are the EDS line spectra of Cu–K and Co–K, respectively.

3.2 The evaluation of catalytic performance

The catalytic performance of the structured Cu@(CuCo-alloy)/Al₂O₃ (Cu/Co=1/2) catalyst was studied in comparison with that of the powdered-CuCo/Al₂O₃ (Cu/Co=1/2) one. As shown in Fig. 4, both catalysts are active in 1-alcohols synthesis, and the total 1-alcohols selectivity (S_{ROH}) increases upon decreasing the reaction temperature. A S_{ROH} value of 50.6% is obtained for Cu@(CuCo-alloy)/Al₂O₃ catalyst at 220 °C, while the maximum S_{ROH} value is only 33.1% for the powdered-CuCo/Al₂O₃ catalyst. In addition, the C₆₊ slate 1-alcohols selectivity in the total 1-alcohols distribution for Cu@(CuCo-alloy)/Al₂O₃ at 220 °C reaches to approximately 48.9%, which is a higher than that of the powdered-CuCo/Al₂O₃ (Cu/Co=1/2) (38.7%). Moreover, it should be noted that CO₂ production is unwanted but frequently reported to be difficult to exclude according.²⁰ As the CO conversion rate increases, an increase of CO₂ production is frequently related to the occurrence of the

Table 1 Catalytic performances of Cu@(CuCo-alloy)/Al₂O₃ catalysts with various Cu/Co ratios and the powdered-CuCo/Al₂O₃ (Cu/Co=1/2) catalyst toward the synthesis of higher alcohols^a

Catalyst	CO conv. (%)	Carbon selectivity (C mol%) ^b			Alcohol Selectivity (wt.) ^c			
		CO ₂	ROH	HC	MeOH	EtOH	C ₃₋₅ OH	C ₆₊ OH
Co/Al ₂ O ₃	36.6	2.3	2.6	95.1	2.3	2.6	27.1	68.0
Cu/Co (1/5)	32.9	4.7	36.2	59.1	15.1	16.8	18.5	49.6
Cu/Co (1/2)	21.5	7.2	50.6	42.2	19.2	16.5	15.4	48.9
Cu/Co (2/1)	20.7	7.9	52.5	39.6	20.9	17.6	22.3	39.2
Cu/Co (5/1)	21.9	8.6	66.8	24.6	66.7	10.3	9.2	13.8
Cu/Al ₂ O ₃	22.3	9.5	86.7	3.8	98.9	0.6	0.3	0.2
powdered-CuCo/Al ₂ O ₃ (1/2)	13.1	9.8	22.9	67.3	22.6	19.8	18.9	38.7

^a Reaction conditions: Temp.=220 °C, P=2 MPa, R(H₂/CO)=2, GHSV=2000 ml/g_{cat}/h.

^b Carbon selectivity is defined as the selectivity of all the carbon-containing products from converted carbon, and the values are recalculated from the original data; HC = total hydrocarbons including methane; ROH = total alcohol including methanol.

^c Alcohol distribution (wt.%): the proportion of each alcohol in the total value.

water-gas shift reaction, $\text{CO} + \text{H}_2\text{O} \rightarrow \text{CO}_2 + \text{H}_2$. In this work, for Cu@(CuCo-alloy)/Al₂O₃, the increase of the CO conversion from 200 to 260 °C does not entail drastic change in the CO₂ production; while predominant CO₂ is produced over powdered-CuCo/Al₂O₃ (Cu/Co=1/2) catalyst in the same temperature range. The most intriguing observation in Fig. 4 is the high α -chain-lengthening probability of 1-alcohol formation for the Cu@(CuCo-alloy)/Al₂O₃ catalyst. The α -value ranges from 0.79 to 0.62 at the reaction temperature between 200 and 280 °C, which therefore achieves the purpose of maximizing the yields of C₆₊ slate 1-alcohols. However, the powdered-CuCo/Al₂O₃ (Cu/Co=1/2) catalyst fails to produce C₆₊ slate 1-alcohols (Fig. 4 and Table 1), with the α -value ranging in 0.68–0.40 at the same reaction temperature. The results indicate that the Cu@(CuCo-alloy)/Al₂O₃ with unique core-shell structure derived from the LDHs precursor exhibits significantly enhanced catalytic behavior.

It is well-known that Cu is the major element for methanol synthesis, serving as the dissociative chemisorption of hydrogen and the associative adsorption of CO; while Co affords the active site of FT function of dissociative CO adsorption (C–C chain growth) and hydrogenation.^{1a,3,7} Accordingly, the synergetic effect of Cu and Co plays a key role in determining the catalytic performance. Therefore, a detailed catalytic performance study of this binary system was performed by changing the relative amount of Cu and Co. As shown in Table 1, the selectivity patterns of various Cu@(CuCo-alloy)/Al₂O₃ catalysts change accordingly. The monometallic Co/Al₂O₃ catalyst exhibits the highest activity in Fischer–Tropsch synthesis producing mostly 95.1% of hydrocarbons with only trace of alcohols (2.6%); while methanol (98.9%) is major reaction product with the lowest selectivity of hydrocarbons for monometallic Cu/Al₂O₃ catalyst. All the CuCo bimetallic catalysts are selective between alcohols and hydrocarbons at 220 °C, i.e., with the increase of Cu/Co ratio, the alcohols selectivity increases while the hydrocarbons selectivity decreases gradually. However, the selectivity of C₆₊ slate 1-alcohols (S_{C₆₊OH}) shows a primary enhancement followed by a sharp decline, and the highest S_{C₆₊OH} value of 48.9% presents in the sample of Cu/Co (1/2), with the S_{ROH} value of 50.6% and S_{CO₂} value of 7.2%. To sum up, a distinct difference in

the performances of these bimetal samples is observed, suggesting a strong copper–cobalt interaction which is responsible for the catalytic selectivity.

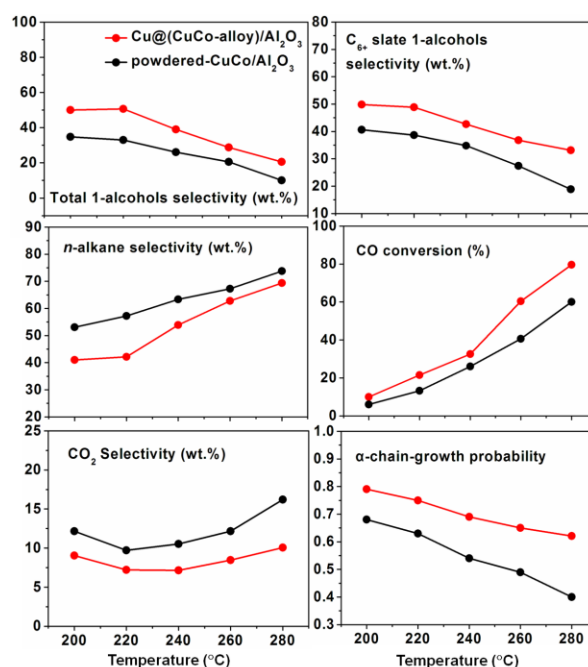


Fig. 4 Catalytic performances of Cu@(CuCo-alloy)/Al₂O₃ (Cu/Co=1/2) and powdered-CuCo/Al₂O₃ (Cu/Co=1/2) catalyst, respectively. Temp.=220 °C, P=2 MPa, GHSV=2000 ml/g_{cat}/h, H₂/CO=2.0. The α -chain-growth probability is calculated according to $\ln(W_n/n) = n \ln \alpha + \ln(1 - \alpha)^2 / \alpha$, in which n is the number of carbon atoms in 1-alcohol and W_n is the weight fraction of 1-alcohol that contains n carbon atoms.

Time-on-stream analysis of the best-performing Cu@(CuCo-alloy)/Al₂O₃ (Cu/Co=1/2) catalyst was investigated at 220 °C with the relative pressure of 2 MPa for up to 48 h as shown in Fig. 5. The catalyst selectivity decreases to a slight extent during the initial 10 h and then maintains at a constant value (43%). This stable activity can be ascribed to the specific core-shell structure of Cu@(CuCo-alloy) NPs in which an unique electronic and geometric interaction between Cu and Co species suppresses the phase separation; the grafting of active NPs into the Al₂O₃ matrix

guarantees a satisfactory stability. Furthermore, the 3D hierarchical Cu@(CuCo-alloy)/Al₂O₃ catalyst provides open tunnels, facilitating the mass diffusion and transportation. HRTEM images of the used Cu@(CuCo-alloy)/Al₂O₃ catalyst are shown in Fig. S2, in which no obvious aggregation is observed and the bimetallic CuCo NPs maintain the core-shell structure with a mean size of 30 nm. In the case of the used powdered-CuCo/Al₂O₃ (Cu/Co=1/2) catalyst however, an increase in the mean size (42 nm) of bimetallic CuCo NPs was observed (Fig. S3).

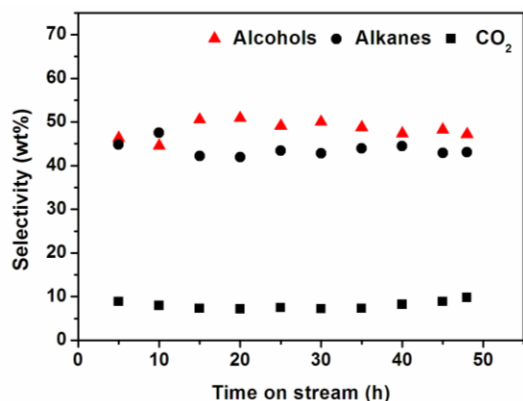


Fig. 5 Product selectivities as a function of time on stream over the Cu@(CuCo-alloy)/Al₂O₃ catalyst (Co/Cu=1/2) performed at 220 °C, 2 MPa and H₂/CO=2.

3.3 Correlation studies on the structure and catalytic behavior

The results above clearly show that the Cu@(CuCo-alloy)/Al₂O₃ catalysts with core-shell structure display excellent catalytic behavior. To give an understanding of structure-performance relationship, XRD, TPR, XPS and FTIR measurements were performed to elucidate the electron and geometry structure for these bimetal catalysts. The nominal and determined metal ratios of the products by inductively coupled plasma emission spectroscopy (ICP-AES) are also summarized in Table S1. Fig. 6 illustrates the XRD patterns of the Cu@(CuCo-alloy)/Al₂O₃ catalysts with various Cu/Co ratios. For the Cu/Co (5/1) sample, the Cu(111) and Co(111) reflection are observed at 2θ 43.3° and 44.3°, respectively, suggesting the separate Cu and Co phase without the formation of a significant degree of solid solution. With the decrease of Cu/Co ratio, the reflections of Cu and Co metal gradually combine together. The Cu/Co (1/5) sample exhibits a single reflection located at between metallic Cu (2θ [111] = 43.3°) and Co (2θ [111] = 44.3°), which implies that Cu atoms are completely incorporated into the Co lattice to the formation of CuCo alloy phase. This result indicates that the degree of alloy can be tuned by changing the Cu/Co ratio in the CuCoAl-LDHs precursor, and a lower Cu/Co ratio facilitates the formation of CuCo alloy. The XRD pattern of used Cu@(CuCo-alloy)/Al₂O₃ (Co/Cu=1/2) catalyst shows that the CuCo alloy phase is stable after the reaction (Fig. S4). As shown in Fig. 7, the Cu NPs in the Cu/Al₂O₃ sample show a particle size of 13.2 nm (Fig. 7A). With the decrease of Cu/Co ratio in the bimetal catalysts, both the particle size and the shell thickness of Cu@(CuCo-alloy) NPs increase in the following order: Cu/Co (2/1) < Cu/Co (1/2) < Cu/Co (1/5) (Fig. 7B–D). The average size of

Cu@(CuCo-alloy) NPs was calculated to be ~9.2, 13.9, and 18.1 nm for Cu/Co (2/1), Cu/Co (1/2), Cu/Co (1/5), with the thickness of ~1.8, 4.1, and 6.2 nm, respectively. In brief, the core-shell structure Cu@(CuCo-alloy)/Al₂O₃ catalysts with various particle size and shell thickness can be obtained by controlling the Cu/Co ratio in CuCoAl-LDHs precursors. The alloy degree and shell thickness will influence the surface composition of catalytic active sites, which will be further studied by the following investigations.

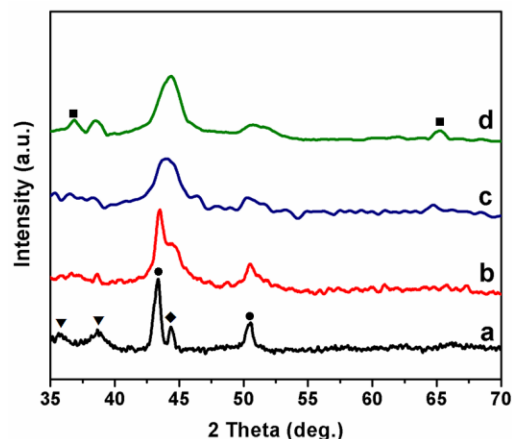


Fig. 6 XRD patterns of Cu@(CuCo-alloy)/Al₂O₃ catalysts with various Cu/Co ratios: (a) Cu/Co=5/1, (b) Cu/Co=2/1, (c) Cu/Co=1/2, (d) Cu/Co=1/5. Crystalline phase: (●) Cu, (◆) Co, (▼) CuO, (■) Co₃O₄.

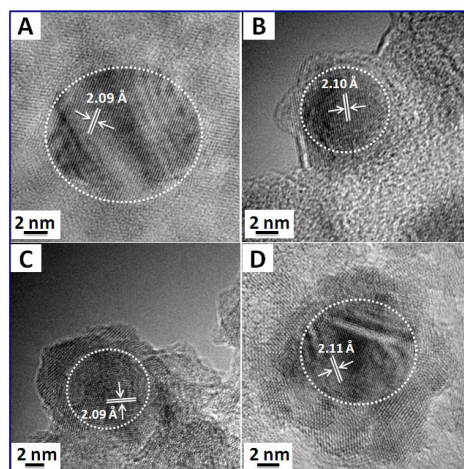


Fig. 7 HRTEM images of the Cu/Al₂O₃ and Cu@(CuCo-alloy)/Al₂O₃ samples with various Cu/Co ratios: (A) Cu/Al₂O₃, (B) Cu/Co=2/1, (C) Cu/Co=1/2, (D) Cu/Co=1/5.

The H₂-TPR measurements were conducted to investigate the reducibility and synergistic effect of Cu–Co in Cu@(CuCo-alloy)/Al₂O₃ samples and the corresponding profiles are shown in Fig. 8. The sample of CuAl-MMO (Fig. 8, curve a) exhibits a main peak at 193 °C, which is attributed to the reduction of CuO to metal Cu,²¹ while the sample of CoAl-MMO sample (Figure 8, curve e) displays two peaks at 371 °C and 568 °C, assigning to the reduction of Co₃O₄ in two steps (Co₃O₄/CoO/Co).²² In the case of CuCoAl-MMO samples (Fig. 8, curve b–d), both the reduction of CuO (in the low temperature range) and Co₃O₄ (in the high temperature range) are observed. Obviously, compared with the CoAl-MMO sample, the broad hydrogen consumption

peak for the reduction of Co_3O_4 shifts to lower temperature (from 568 °C to 359 °C) along with the increase of Cu content (from Cu/Co=0/1 to Cu/Co=5/1), indicating a Cu-promoted reduction of Co species to produce CuCo alloy.²³ However, the H_2 consumption peak of CuO phase shifts gradually to higher temperature (from 193 °C to 279 °C) along with the increase of Co content (from Cu/Co=1/0 to Cu/Co=1/2). The results suggest a strong synergistic effect between copper and cobalt occurs in the reduction process of CuCoAl-MMO samples.^{22,24}

To further confirm the formation of the core-shell structure and the active site state of the $\text{Cu}@\text{(CuCo-alloy)}/\text{Al}_2\text{O}_3$ catalyst, XPS measurements were performed. For all the sample, two peaks (Fig. 9A) centered at ~931.9 and 951.5 eV are mainly ascribed to Cu $2p_{3/2}$ and Cu $2p_{1/2}$ peaks of Cu^0 and/or Cu^+ , respectively, which is difficult to differentiate these two species based on their Cu $2p$ binding energies.²⁴ Therefore, the Modified Auger parameter (α') was used to distinguish Cu^0 from Cu^+ species, which is an important energy parameter for identifying the chemical state of elements where chemical shift is very small or comparable with the energy resolution of the instrument.¹⁵ As shown in Table S2, the Modified Auger parameter for the $\text{Cu}@\text{(CuCo-alloy)}/\text{Al}_2\text{O}_3$ samples with various Cu/Co ratios is close to the reported value for Cu^0 (~1851.3 eV).²⁵ For the used $\text{Cu}@\text{(CuCo-alloy)}/\text{Al}_2\text{O}_3$ (Co/Cu=1/2) catalyst (Fig. S6), the Cu LMM XAES spectrum shows an Auger peak of Cu^+ (~915.6 eV) besides that of Cu^0 .²⁶ However, the Modified Auger parameter is ~1851.2 eV, indicating only slight Cu^0 specie is oxidized during the reaction process.²⁵ For the Co $2p$ XPS spectra of fresh and used $\text{Cu}@\text{(CuCo-alloy)}/\text{Al}_2\text{O}_3$ catalyst (Fig. 10 and Fig. S8), a broad peak in the range 775–785 eV is observed, which is difficult to determine the chemical state of Co species.²⁷ However, the Modified Auger parameter for these samples ranges in 1550.9–1552.2 eV (Table S2), close to the reported value for Co^0 (~1551.2 eV) other than Co^{2+} (~1553.8 eV).²⁸ This indicates that Co^0 is the predominant species both in the fresh and used $\text{Cu}@\text{(CuCo-alloy)}/\text{Al}_2\text{O}_3$ catalyst and the structure of CuCo alloy shell remains stable during the reaction process. As listed in Table 2,

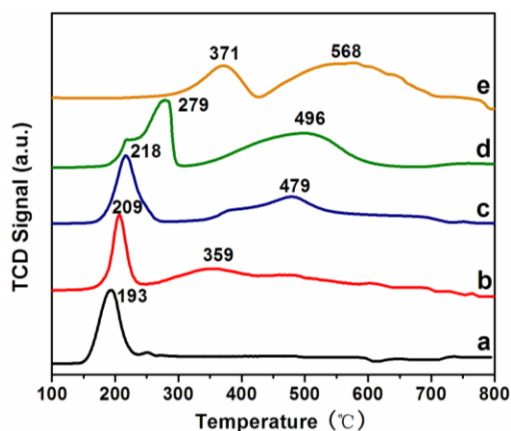


Fig. 8 H_2 -TPR profiles of CuAl-MMO, CoAl-MMO and CuCoAl-MMO samples with various Cu/Co ratios: (a) CuAl-MMO, (b) Cu/Co=5/1, (c) Cu/Co=2/1, (d) Cu/Co=1/2 and (e) CoAl-MMO.

the Cu/Co ratio at surface (2.88/1.00) is much smaller than the bulk ratio for the Cu/Co (4.81/1.00) sample, indicating the

existence of predominant Co metal in the shell section. Notably, the surface Cu/Co ratio is bigger than the bulk ratio for the Cu/Co (2/1) sample, which is indicative of the migration of copper atom to the crystallite surface to form a CuCo alloy shell. It is therefore reasonable to conclude that the reduced bimetal NPs possess a core-shell structure, with predominant Cu in the core and CuCo alloy in the outer shell. Furthermore, it was worth noting that the Cu $2p_{3/2}$ peak shifts from 931.9 (Cu-only) to 932.4 eV upon alloying with increased Co (Cu/Co=1/5) (Fig. 9, from curve e to a); while a shift from 780.9 (Co-only) to 780.0 eV (Cu/Co=2/1) can be observed for the Co $2p_{3/2}$ peak (Fig. 10, from curve a to d). An upshift of Co $2p_{3/2}$ is not observed for Cu/Co (5/1) sample (Fig. 10, curve e), probably due to a portion of unalloyed Co. This indicates the diminishing electron density in the Cu^0 nucleus, resulting from the electron scavenging property of Co^0 .²⁹ Therefore, a strong electron interaction between Cu and Co occurs on the catalyst surface, wherein electrons likely transfer from Cu species to Co species in the bimetal $\text{Cu}@\text{(CuCo-alloy)}/\text{Al}_2\text{O}_3$ catalyst.

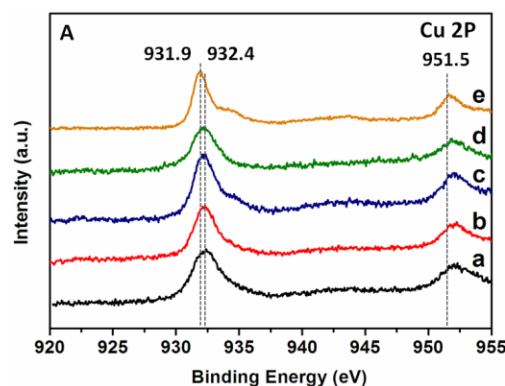


Fig. 9 Cu XPS spectra of $\text{Cu}/\text{Al}_2\text{O}_3$ and $\text{Cu}@\text{(CuCo-alloy)}/\text{Al}_2\text{O}_3$ samples with various Cu/Co ratios: (a) Cu/Co=1/5, (b) Cu/Co=1/2, (c) Cu/Co=2/1, (d) Cu/Co=5/1, (e) $\text{Cu}/\text{Al}_2\text{O}_3$.

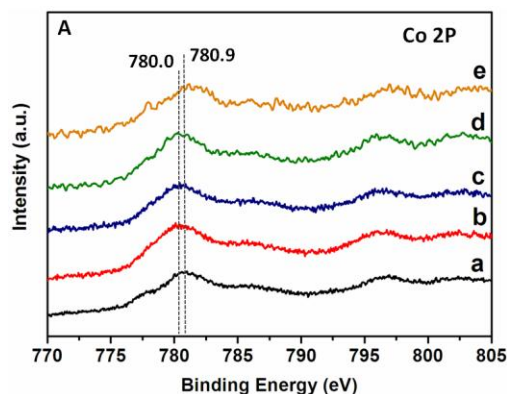


Fig. 10 Co XPS spectra of (a) $\text{Co}/\text{Al}_2\text{O}_3$ and $\text{Cu}@\text{(CuCo-alloy)}/\text{Al}_2\text{O}_3$ samples with various Cu/Co ratios: (b) Cu/Co=1/5, (c) Cu/Co=1/2, (d) Cu/Co=2/1, (e) Cu/Co=5/1.

In situ FTIR is a useful surface-sensitive technique to study the adsorption behavior of catalysts under reaction conditions and to elucidate the nature of the active sites and the surface intermediates involved in the reaction. Fig. 11 displays IR spectra of CO adsorbed on $\text{Co}/\text{Al}_2\text{O}_3$ and $\text{Cu}@\text{(CuCo-alloy)}/\text{Al}_2\text{O}_3$ samples with different Cu/Co ratios (5/1, 2/1, 1/2, 1/5). The IR spectra of $\text{Co}/\text{Al}_2\text{O}_3$, bimetallic Cu/Co (1/5) and Cu/Co (1/2)

Table 2 Cu/Co ratio at the surface and in the bulk for the bimetal Cu@(CuCo-alloy)/Al₂O₃ catalysts

Nominal ratio	molar Cu/Co ratio	
	Bulk (ICP)	Surface (XPS)
Cu/Co (5/1)	4.81/1.00	2.88/1.00
Cu/Co (2/1)	1.96/1.00	2.07/1.00
Cu/Co (1/2)	1.00/2.63	1.00/2.86
Cu/Co (1/5)	1.00/4.76	1.00/5.02

catalyst (with predominant Co) exhibit strong bands with maximum at 1991, 1980, and 1959 cm⁻¹, respectively, which can be assigned to the bridge-type adsorbed CO on Co metal sites.³⁰ In comparison with the monometallic Co/Al₂O₃ catalyst (1991 cm⁻¹), the significant shifting of this peak to lower frequencies (from 1991 to 1959 cm⁻¹) for the bimetallic samples along with the increase of Cu content indicates the surface Co species is slightly negatively charged.^{29b} That is, electron transfer from surface Cu species to Co species occurs, as also supported by the XPS data discussed above. Upon further increasing the Cu content (Cu/Co=2/1 sample: Fig. 11, curve d), the bridge-type adsorbed CO disappears completely, while the linearly adsorbed CO on Co metal is observed. The peak fitting of the band observed in this region reveals the presence of two different peaks (2015 and 2038 cm⁻¹), which point to different Co⁰ sites. The Co-carbonyl band at 2015 cm⁻¹ can be ascribed to coordinatively unsaturated Co⁰ sites such as those located in steps or corners; while the contribution at 2038 cm⁻¹ can be attributed to Co⁰ sites located in planar (terrace) positions.³¹ In addition, the IR spectra of CO adsorbed on Cu/Co (1/2), Cu/Co (2/1), and Cu/Co (5/1) samples (Fig. 11, curve c, d, e) shows an absorption band at 2085, 2095 and 2096 cm⁻¹, respectively, accompanying with gradually enhanced intensity, which points to the Cu⁰ surface site.³² In addition, this peak shifts to higher frequencies (from 2085 to 2096 cm⁻¹) along with the increase of Cu content, further indicating the electron transfer from surface Cu species to Co species. It can be seen from Fig. 11 that the CO adsorption state on Co⁰ species gradually transfers from bridge-type to linear-type along with the increase of Cu content, which can be ascribed to “active-site isolation” effect³³ imposed by Cu and thus a close interaction of Cu⁰ and Co⁰ species.

Previous researchers have concluded that the linearly-adsorbed CO is the active site for the formation of oxygenated compounds, while the bridge-type adsorbed CO leads toward formation of hydrocarbon compounds, since the latter one has a weaker C–O bond and thus can be more easily hydrogenated.^{29b,34} The catalytic evaluation results (Table 1) show that the Co-rich catalysts (Co/Al₂O₃, Cu/Co (1/5) with dominated bridge-type adsorption) are more selective toward hydrocarbons; while the Cu-rich catalysts (Cu/Co (2/1), Cu/Co (5/1) with dominated linear-type adsorption) are prone to obtain oxygenated compounds. According to the reaction pathway for CO hydrogenation over the CuCo-based catalysts (Fig. S9),^{1a,3,7} Cu is the major element for methanol synthesis, serving as the associative adsorption of CO; while Co affords the active site of FT function of dissociative CO adsorption and hydrogenation. A synergistic effect between these two metal compositions is believed to be essential in this reaction. For the Cu@(CuCo-

alloy)/Al₂O₃ (Cu/Co=1/2) catalyst, copper species provides active site for the associative adsorption of CO to produce CO*; while cobalt species acts as active site for CO dissociation, C–C chain growth and hydrogenation to form *C_nH_z group. The CO* moves to the *C_nH_z group and inserts *via* surface migration over a short distance between Co and Cu site and subsequent hydrogenation to produce higher alcohols.^{3,7} A homogeneous distribution of copper and cobalt as well as their distance (geometric properties) are necessary to obtain higher alcohols. For the electron interaction between Cu and Co, the electron transfer from Cu to Co increases the electron density of Co, which weakens the C–O bond of the adsorbed CO and facilitates its dissociation; while the decreased electron density of Cu enhances the associative adsorption of CO.³⁵ Therefore, both the geometric effect and electronic effect between Co and Cu contribute to the enhancement of selectivity toward higher alcohols.

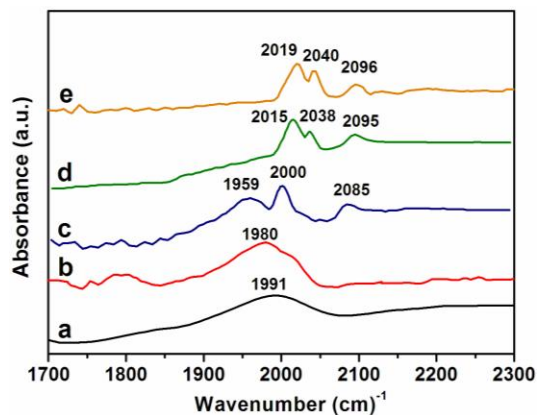


Fig. 11 *In situ* FTIR spectra of CO adsorption on (a) Co/Al₂O₃, and Cu@(CuCo-alloy)/Al₂O₃ samples with various Cu/Co ratios: (b) Cu/Co=1/5, (c) Cu/Co=1/2, (d) Cu/Co=2/1, (e) Cu/Co=5/1.

4. Conclusions

In summary, a structured core-shell Cu@(CuCo-alloy)/Al₂O₃ catalyst was fabricated *via* a facile two-step procedure: the direct growth of CuCoAl-LDHs nanoplatelets on aluminum substrates followed by a calcination-reduction process, which serves as an efficient catalyst toward the CO hydrogenation (CO conversion: 21.5%; C₆₊ slate 1-alcohols selectivity: 48.9%). The specific core-shell structure Cu@(CuCo-alloy) NPs possess a Cu-rich core and a CuCo-alloy shell, which improves the electronic/geometric interaction between Cu and Co and effectively avoids phase separation during the catalytic reaction. In addition, the open channels associated with the hierarchical structure facilitate the mass diffusion/transport as well as inhibit the formation of hotspots. This strategy can be extended to synthesize other bimetallic catalysts derived from LDHs and offers new opportunities for achieving largely enhanced catalytic performances based on bimetal synergistic effect.

90 Acknowledgements

This work was supported by the 973 Program (Grant no. 2011CBA00504), the National Natural Science Foundation of China (NSFC), the Beijing Natural Science Foundation

(2132043), the Research on the Chemical Industry Cluster and the Socioeconomic Coordinated Development of Xinjiang (Grant no. JX20140015). M. Wei particularly appreciates the financial aid from the China National Funds for Distinguished Young Scientists of the NSFC.

Notes and references

^a State Key Laboratory of Chemical Resource Engineering, Beijing University of Chemical Technology, Beijing, 100029, China. E-mail: weimin@mail.buct.edu.cn; Fax: +86-10-64425385; Tel: +86-10-

64412131

^b Photochemical Conversion and Optoelectronic Materials, Technical Institute of Physics and Chemistry, Chinese Academy of Sciences, Beijing, P. R. China.

[‡]These authors contributed equally.

15

- 1 (a) J. J. Spivey and A. Egbebi, *Chem. Soc. Rev.*, 2007, **36**, 1514; (b) V. Subramani and S. K. Gangwal, *Energy Fuels*, 2008, **22**, 814; (c) M. Behrens, F. Studt, I. Kasatkin, S. Kuhl, M. Havecker, F. Abild-Pedersen, S. Zander, F. Girgsdies, P. Kurr, B. L. Kniep, M. Tovar, R. W. Fischer, J. K. Nørskov and R. Schlogl, *Science*, 2012, **336**, 893; (d) S. Zander, E. L. Kunkes, M. E. Schuster, J. Schumann, G. Weinberg, D. Teschner, N. Jacobsen, R. Schlogl and M. Behrens, *Angew. Chem., Int. Ed.*, 2013, **52**, 6536; (e) N. Yan, C. Zhao, C. Luo, P. J. Dyson, H. Liu and Y. Kou, *J. Am. Chem. Soc.*, 2006, **128**, 8714.
- 2 (a) M. Gupta, M. L. Smith and J. J. Spivey, *ACS Catal.*, 2011, **1**, 641; (b) M. R. Morrill, N. T. Thao, H. Shou, R. J. Davis, D. G. Barton, D. Ferrari, P. K. Agrawal and C. W. Jones, *ACS Catal.*, 2013, **3**, 1665; (c) J. Wang, P. A. Chernavskii, A. Y. Khodakov and Y. Wang, *J. Catal.*, 2012, **286**, 51; (d) V. R. Calderone, N. R. Shiju, D. C. Ferre and G. Rothenberg, *Green Chem.*, 2011, **13**, 1950.
- 3 K. Fang, D. Li, M. Lin, M. Xiang, W. Wei and Y. Sun, *Catal. Today*, 2009, **147**, 133.
- 4 (a) N. D. Subramanian, G. Balaji, C. S. S. R. Kumar and J. J. Spivey, *Catal. Today*, 2009, **147**, 100; (b) J. Wang, P. A. Chernavskii, Y. Wang and A. Y. Khodakov, *Fuel*, 2013, **103**, 1111; (c) W. Gao, Y. Zhao, J. Liu, Q. Huang, S. He, C. Li, J. Zhao and M. Wei, *Catal. Sci. Technol.*, 2013, **3**, 1324.
- 5 (a) X. Peng, Q. Pan and G. L. Rempel, *Chem. Soc. Rev.*, 2008, **37**, 1619; (b) F. F. Tao, S. Zhang, L. Nguyen and X. Zhang, *Chem. Soc. Rev.*, 2012, **41**, 7980; (c) T. Deng and H. Liu, *Green Chem.*, 2013, **15**, 116.
- 6 H. Wang, W. Zhou, J. X. Liu, R. Si, G. Sun, M. Q. Zhong, H. Y. Su, H. B. Zhao, J. A. Rodriguez, S. J. Pennycook, J. C. Idrobo, W. X. Li, Y. Kou and D. Ma, *J. Am. Chem. Soc.*, 2013, **135**, 4149.
- 7 G. Prieto, S. Beijer, M. L. Smith, M. He, Y. Au, Z. Wang, D. A. Bruce, K. P. de Jong, J. J. Spivey and P. E. de Jongh, *Angew. Chem., Int. Ed.*, 2014, **53**, 6397.
- 8 K. Xiao, X. Qi, Z. Bao, X. Wang, L. Zhong, K. Fang, M. Lin and Y. Sun, *Catal. Sci. Technol.*, 2013, **3**, 1591.
- 9 (a) X. Du, D. Zhang, L. Shi, R. Gao and J. Zhang, *Nanoscale*, 2013, **5**, 2659; (b) V. C. Deborah, A. P. Carlos, M. M. S. Vera and S. Martin, *Appl. Catal., A*, 1999, **176**, 205.
- 10 (a) G. R. Williams and D. O'Hare, *J. Mater. Chem.*, 1996, **16**, 3065; (b) A. M. Fogg, A. L. Rohl, G. M. Parkinson and D. O'Hare, *Chem. Mater.*, 1999, **11**, 1194; (c) L. Li, Y. Feng, Y. Li, W. Zhao and J. Shi, *Angew. Chem., Int. Ed.*, 2009, **48**, 5888; (d) S. He, S. Zhang, J. Lu, Y. Zhao, J. Ma, M. Wei, D. G. Evans and X. Duan, *Chem. Commun.*, 2011, **47**, 10797.
- 11 (a) A. Ota, E. L. Kunkes, I. Kasatkin, E. Groppo, D. Ferri, B. Poceiro, Y. R. M. Navarro and M. Behrens, *J. Catal.*, 2012, **293**, 27; (b) M.-Q. Zhao, Q. Zhang, X. L. Jia, J. Q. Huang, Y. H. Zhang and F. Wei, *Adv. Funct. Mater.*, 2010, **20**, 677; (c) M. Q. Zhao, Q. Zhang, J. Q. Huang and F. Wei, *Adv. Funct. Mater.*, 2012, **22**, 675.
- 12 (a) S. Xia, R. Nie, X. Lu, L. Wang, P. Chen and Z. Hou, *J. Catal.*, 2012, **296**, 1; (b) M. Behrens, I. Kasatkin, S. Kuhl and G. Weinberg, *Chem. Mater.*, 2010, **22**, 386; (c) S. Y. Zhang, G. L. Fan and F. Li, *Green Chem.*, 2013, **15**, 2389; (d) H. Liu and E. Min, *Green Chem.*, 2006, **8**, 657.

- 13 (a) M. Q. Zhao, Q. Zhang, W. Zhang, J. Q. Huang, Y. Zhang, D. S. Su and F. Wei, *J. Am. Chem. Soc.*, 2010, **132**, 14739; (b) S. He, Z. An, M. Wei, D. G. Evans and X. Duan, *Chem. Commun.*, 2013, **49**, 5912; (c) S. He, C. Li, H. Chen, D. Su, B. Zhang, X. Cao, B. Wang, M. Wei, D. G. Evans and X. Duan, *Chem. Mater.*, 2013, **25**, 1040; (d) W. Gao, C. Li, H. Chen, M. Wu, S. He, M. Wei, D. G. Evans and X. Duan, *Green Chem.*, 2014, **16**, 1560.
- 14 (a) J. Liu, Y. Li, X. Huang, G. Li and Z. Li, *Adv. Funct. Mater.*, 2008, **18**, 1448; (b) H. Chen, F. Zhang, S. Fu and X. Duan, *Adv. Mater.*, 2006, **18**, 3089.
- 15 (a) G. Moretti, *J. Electron Spectrosc.*, 1998, **95**, 95; (b) G. Moretti, *Surf. Sci.*, 2013, **618**, 3.
- 16 Z. Sun, L. Jin, S. He, Y. Zhao, M. Wei, D. G. Evans and X. Duan, *Green Chem.*, 2012, **14**, 1909.
- 17 (a) Y. Xiang, V. Chitry, P. Liddicoat, P. Felfer, J. Cairney, S. Ringer and N. Kruse, *J. Am. Chem. Soc.*, 2013, **135**, 7114; (b) C. N. Avila-Neto, D. Zanchet, C. E. Hori, R. U. Ribeiro and J. M. C. Bueno, *J. Catal.*, 2013, **307**, 222.
- 18 N. Barrabes, D. Comado, K. Foettinger, A. Dafinov, J. Llorca, F. Medina and G. Rupprechter, *J. Catal.*, 2009, **263**, 239.
- 19 (a) Y. Song, H. Modrow, L. L. Henry, C. K. Saw, E. E. Doomes, V. Palshin, J. Holmes and C. S. S. R. Kumar, *Chem. Mater.*, 2006, **18**, 2817; (b) G. Ennas, A. Falqui, G. Paschina and G. Marongiu, *Chem. Mater.*, 2005, **17**, 6486; (c) X. Xie, Y. Li, Z. Q. Liu, M. Haruta and W. Shen, *Nature*, 2009, **458**, 746.
- 20 C. Philipp, D. D. Courty, F. Edouard and S. Andre, *J. Mol. Catal.*, 1982, **17**, 241.
- 21 (a) S. Wang, Y. Zhang and H. Liu, *Chem.-Eur. J.*, 2010, **5**, 1100; (b) W. Tong, A. West, K. Cheung, K. M. Yu and S. C. E. Tsang, *ACS Catal.*, 2013, **3**, 1231.
- 22 (a) A. M. Karim, Y. Su, M. H. Engelhard, D. L. King and Y. Wang, *ACS Catal.*, 2011, **1**, 279; (b) J. L. Ewbank, L. Kovarik, C. C. Kenvin and C. Sievers, *Green Chem.*, 2014, **16**, 885.
- 23 C. N. Ávila-Neto, D. Zanchet, C. E. Hori, R. U. Ribeiro and J. M. C. Bueno, *J. Catal.*, 2013, **307**, 222.
- 24 B. Bridier and J. Perez-Ramirez, *J. Am. Chem. Soc.*, 2010, **132**, 4321.
- 25 (a) J. P. Espino s, J. Morales, A. Barranco, A. Caballero, J. P. Holgado and A. R. Gonza lez-Elipe, *J. Phys. Chem. B*, 2002, **106**, 6921; (b) M. C. Biesinger, L. W. M. Lau, A. R. Gerson and R. St. C. Smart, *Appl. Surf. Sci.*, 2010, **257**, 887.
- 26 (a) J. Gong, H. Yue, Y. Zhao, S. Zhao, L. Zhao, J. Lv, S. Wang and X. Ma, *J. Am. Chem. Soc.*, 2012, **134**, 13922; (b) K. M. Yu, W. Tong, A. West, K. Cheung, T. Li, G. Smith, Y. Guo and S. C. Tsang, *Nat. Commun.*, 2012, **3**, 1230.
- 27 B. Bayram, I. I. Soykal, D. von Deak, J. T. Miller and U. S. Ozkan, *J. Catal.*, 2011, **284**, 77.
- 28 (a) A. Sharma, S. Tripathi and T. Shripathi, *Appl. Surf. Sci.*, 2009, **256**, 530; (b) J. Zhao, L. K. Ballast, T. Z. Hossain, R. E. Trostell and W. C. Bridgman, *J. Vac. Sci. Technol. A*, 2000, **18**, 1690.
- 29 (a) A. Yin, C. Wen, X. Guo, W. L. Dai and K. Fan, *J. Catal.*, 2011, **280**, 77; (b) F. Morales, E. Desmit, F. Degroot, T. Visser and B. Weckhuysen, *J. Catal.*, 2007, **246**, 91.
- 30 A. Y. Khodakov, J. Lynch, D. Bazin, B. Rebours, N. Zanier, B. Moisson and P. Chaumette, *J. Catal.*, 1997, **168**, 16.
- 31 G. Prieto, P. Concepción, R. Murciano and A. Martínez, *J. Catal.*, 2013, **302**, 37.
- 32 A. G. Sato, D. P. Volanti, D. M. Meira, S. Damyanova, E. Longo and J. M. C. Bueno, *J. Catal.*, 2013, **307**, 1.
- 33 (a) Y. Somanoto and W. M. H. Sachtler, *J. Catal.*, 1974, **32**, 315; (b) Y. He, L. Liang, Y. Liu, J. Feng, C. Ma and D. Li, *J. Catal.*, 2014, **309**, 166.
- 34 (a) N. Kumar, M. L. Smith and J. J. Spivey, *J. Catal.*, 2012, **289**, 218; (b) N. Tsubaki, *J. Catal.*, 2001, **199**, 236; (c) H. Xiong, Y. Zhang, K. Liew and J. Li, *J. Mol. Catal. A*, 2008, **295**, 68.
- 35 (a) B. Qiao, A. Wang, X. Yang, L. F. Allard, Z. Jiang, Y. Cui, J. Liu, J. Li and T. Zhang, *Nat. Chem.*, 2011, **3**, 634; (b) R. Ramamoorthy and R. D. Gonzalez, *J. Catal.*, 1979, **58**, 188; (c) Y. Zhao, S. Li and Y. Sun, *J. Phys. Chem. C*, 2013, **117**, 24920; (d) V. Schwartz, A. Campos, A. Egbebi, J. J. Spivey and S. H. Overbury, *ACS Catal.*, 2011, **1**, 1298.

Core–Shell Cu@(CuCo -alloy)/ Al_2O_3 Catalysts for the Synthesis of Higher Alcohols from Syngas

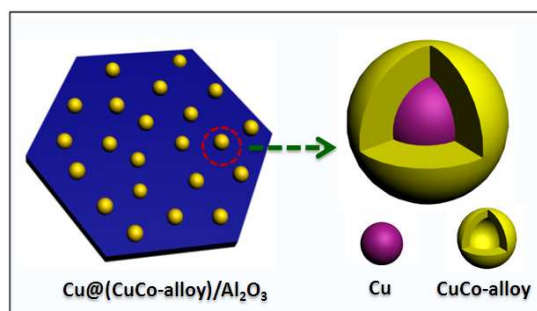
Wa Gao,^{‡a} Yufei Zhao,^{‡b} Haoran Chen,^a Hao Chen,^a Yinwen Li,^a Shan He,^a Yingkui Zhang,^a Min Wei,^{*a} David G. Evans^a and Xue Duan^a

^a State Key Laboratory of Chemical Resource Engineering, Beijing University of Chemical Technology, Beijing, 100029, China. E-mail: weimin@mail.buct.edu.cn

^b Photochemical Conversion and Optoelectronic Materials, Technical Institute of Physics and Chemistry, Chinese Academy of Sciences, Beijing, P. R. China.

[‡] These authors contributed equally.

Graphical Abstract



Core–shell $\text{Cu} @ (\text{CuCo}\text{-alloy}) / \text{Al}_2\text{O}_3$ catalysts were fabricated *via* a facile two-step procedure: *in situ* growth of CuCoAl -LDH nanoplatelets on aluminum substrates followed by a calcination-reduction process, which exhibit excellent catalytic behavior toward CO hydrogenation to produce higher alcohols.